Shock-Ionized Jets from Massive Protostars

A Technical Report submitted to the Department of Astronomy

Presented to the Faculty of the School of Engineering and Applied Science

University of Virginia • Charlottesville, Virginia

In Partial Fulfillment of the Requirements for the Degree

Bachelor of Science, School of Engineering

Emiko Gardiner

Spring, 2022

Technical Project Team Members

Jan Staff

Jonathan Ramsey

On my honor as a University Student, I have neither given nor received unauthorized aid on this assignment as defined by the Honor Guidelines for Thesis-Related Assignments

Jonathan Tan, Department of Astronomy

Shock-Ionized Jets From Massive Protostars

Emiko C. Gardiner[1]

[1] *School of Engineering and Applied Science, University of Virginia, Charlottesville, VA 22903, USA*

ABSTRACT

Many stars launch magnetically- and accretion-powered outflows during their formation. Such outflows may play crucial roles in regulating the growth of the protostar, and through the injection of energy and momentum into the surroundings, also the birth of any surrounding star cluster. In the case of massive stars, these intense outflows can also provide important diagnostic information on the protostellar accretion mechanism. Here we calculate the shock heating and resulting radio emission in numerical models of outflows along the evolutionary sequence of massive star formation within the framework of the "Turbulent Core Model". We post-process 3D magneto-hydrodynamic simulation snapshots of a magneto-centrifugally launched disk wind from a massive protostar up to $24M_\odot$ that interacts with the protostellar envelope, and calculate shock temperatures, ionization fractions and radio free-free emission in the outflow. We find heating up to ∼10 million degrees K in the shocks at the interface between outflow cavity and the infalling envelope, which we find results in near complete ionization. However, line-of-sight averaged ionization fractions peak around ∼10%, in agreement with values recently reported from observations of the massive protostar G35.20-0.74N. By calculating radio continuum intensity maps and spectra, we further compare our results with observations of massive protostars, finding good agreement in the radio versus bolometric luminosity diagram up to values of about 10,000 solar luminosities. At higher luminosities, contributions from photoionization may become dominant. Finally, our model exhibits 10-year radio flux variability of ∼10% for the inner 1000 au region, comparable to observed levels in some hyper-compact HII regions.

Keywords: stars: formation - stars: massive - ISM: jets and outflows - radio continuum

1. INTRODUCTION

Massive stars fundamentally influence galaxy evolution by ionizing their surrounding gas and enriching the interstellar medium with heavy elements. Yet, no consensus has been reached on their formation process because massive stars are difficult to observe. They are rare in comparison with low mass stars, their formation sites are distant, and they form embedded in dense gas and dust. More visible, however, are the accretion-powered bipolar jets, parallel to those typical to the low-mass case. Several observations have been made of similar outflows being observed from massive star forming regions, such as G35.2/0.74 N. In low-mass stars collimated jets are a result of magneto-centrifugal forces launching material from the star and inner circumstellar disk along magnetic field surfaces, thereby extracting angular momentum from the system (Bacciotti 2004). We investigate whether the outflows from massive stars follow the same disk-wind driven model, and thus whether their formation follows the same model.

Several formation scenarios have been proposed, with leading theories falling into the classes of *Core Accretion* and *Competitive Accretion*. Core Accretion offers a scaled-up version of the standard low-mass formation process, in which self-gravity drives the formation of a concentrated core onto which matter accretes (Shu et al. 1987). The Turbulent Core Model resolves discrepancies between the low and high mass cases as turbulence within the cores drives an increase in accretion rate over time (McKee & Tan 2003). Alternatively, Competitive Accretion argues that several protostars form within a clump, with the innermost becoming the largest and the oldest becoming the most gravitationally attractive. In this model, simulated by Bonnell et al. (1997), the protostar is 'clump-fed' as it moves throughout the clump, as opposed to feeding from the single coherent core of Core Accretion. Competitive Accretion-based models like that of Wang et al. (2010) have demonstrated poor accretion rates, too low by an order of magnitude even for the most massive (46 $M_\odot$) star of the clump. A third model is that of coalescence, in which multiple lower-mass stars merge to form a massive star. However, this model depends upon atypically high stellar densities.

The mechanism behind the molecular outflows observed in massive star-forming regions is still under debate. Understanding this mechanism is crucial not only to testing accretion models, but also to understanding how massive protostars impact their environment, such as through outflow-envelope interactions, outflow-core interactions, outflowcloud interactions far from the source, and shock chemistry (Arce et al. 2007). Proposed models fall into the four classes (Cabrit et al. 1997): Wind-driven shells (Shu et al., 1991; Li and Shu, 1996; Matzner and McKee, 1999), jet-driven bow shocks t (Raga and Cabrit, 1993; Masson and Chernin, 1993), jet-driven turbulent flows (Canto and Raga, 1991; Raga et al., 1993; Stahler, 1994; Lizano and Giovanardi, 1995; Canto´et al., 2003, and references therein)., and circulation flows (Fiege and Henriksen, 1996a,b).

Simulations offer a practical means to test the accretion models that might produce observed outflows. We simulate the disk-wind model developed by Blandford & Payne (1982) as the outflow mechanism fitting with the turbulent core model of core accretion. Disk-wind driven models have been tested numerically (Staff et al. 2019), but to test these simulations against observations, we require observable quantities, primarily radio emissions because they can penetrate the gas and dust that obscures massive star-forming regions. Sources of outflow emissions include shock ionization, photoionization (Tanaka et al. 2016), and dust heating. We focus on shock ionization, because the extreme velocity gradient between the outflow's jet and it's surrounding envelope yields highly ionized regions that can produce strong radio emissions.

In this paper, we post-process snapshot data of a protostellar outflow simulation to model shocks in the jet; predict observables including ionization fraction, intensity of radio emission, spectra, and flux variability; and compare these predicted observables to observations and theory. The structure of the paper is as follows. In §2 we describe the simulation structure, calculations of shock parameters, and methods for predicting emissions. In §3 we present the simulation and shock-modeling results, in §4 we discuss these results in comparison to observations and caveats of the simulation, and in §5 we summarize the key takeaways.

2. METHODS

2.1. *MHD Simulation Details*

The post-processing analysis that we present in this paper uses snapshots from a 3D, ideal magneto-hydrodynamic (MHD) simulation of a protostellar outflow interacting with a surrounding natal envelope. The simulation domain includes one hemisphere of the protostar + outflow system, from 100 au above the accretion disk mid-plane, up to a height of $25,000$ au (see Staff et al. 2019, , Staff et al. 2021 in preparation for details and justification). The outflow is injected using a nozzle-like prescription into the simulation box at the lower z boundary. Mass can accrete from the envelope by flowing out of the lower z boundary, and this accreted mass results in the star and accompanying accretion disk growing (see Staff et al. 2021, in preparation). The rate at which mass flows through the z boundary is constrained so that the growth rate of the star with time matches the results of Zhang et al. (2014). Outflow boundary conditions allowing mass to flow out are used at all the other boundaries.

As the star grows, the mass flow and momentum rates of the outflow also changes with time, following Zhang et al. (2014). Initially, the envelope mass is set to 60 $M_\odot$ and a radius of $\sim 12,000$ au. The envelope is initialized with a power-law dependence on according to $\rho \propto r^{-3/2}$ (McKee & Tan 2003). The simulation starts with a 1 $M_\odot$ protostar at the center of the envelope, it begins to collapse under the force of gravity, and the accretion of envelope material and the propagation of the outflow is simulated for 100,000 years, at which point the star has grown to more than 25 $M_\odot$ (Staff et al. 2021, in preparation).

The simulation was run using ZEUS-MP Norman (2000), using an isothermal equation of state with a fixed sound speed of 0.9 km s^{-1}. The simulations use a logarithmically stretched grid in all three dimensions, consisting of $168 \times 280 \times 280$ grid cells. Cells are smallest near the outflow axis and near the lower x_1 boundary. In the simulation snapshots we employed, the minimum cell size is $\sim$12 au. The initial core is threaded by a "Blandford-Payne" like poloidal magnetic field (Blandford & Payne 1982) plus a constant field added to it to ensure a core flux of ~ 1 mG.

2.2. *Calculating Shock Temperatures and Ionization Fractions*

We performed a post processing analysis of the MHD simulation snapshots to model shock-ionization and the resulting emissions. First we calculated the shock velocities, used those to calculate post-shock temperatures, and used the temperatures to calculate ionization fractions. Given the temperatures and ionization fractions, we calculated emission coefficients, absorption coefficients, and optical depth. These solved the 1-D radiative transfer equation to find intensity of radio emissions, which was then integrated to determine radio flux. We refer to coordinates (z, x, y) indexed by (i, j, k) with z being the outflow direction. The methods are given generally for emissions in any axial direction and the results are shown specifically for y being the line of sight direction, to map x-z plane projections. The gas density and velocity provided by the simulation output were used to calculate all necessary quantities as follows.

Shock velocities were found by taking, at each face of a cell, the velocity difference between each cell and its neighbors, modulo only using converging velocity components. This yielded the inward velocity to the current cell, in the reference frame of that cell. If this value was net positive in the inward direction (i.e. converging), it was set as the shock velocity at that face, otherwise we did not consider a shock at that face. While these velocity differences are only true shock velocities if larger than the sound speed, applying the shock calculation to lower values gives a negligible contribution to the temperature. This process was replicated for every cell.

Given the shock velocities, a post-shock temperature was calculated for the shock at each face, according to the standard Rankine-Hugoniot shock jump conditions for the case that the Mach number, M, is $\gg 1$, as

$$T = \frac{2(\gamma-1)}{(\gamma+1)^2}\frac{\mu v_s^2}{k_B} = \frac{3}{16}\frac{\mu v_s^2}{k} = (1.38\times10^7)\Big(\frac{\mu/m_H}{1.4/2.3}\Big)\Big(\frac{v_s}{1000\mathrm{km/s}}\Big)^2\mathrm{K}. \tag{1}$$

in which in which $\gamma = \frac{5}{3}$ represents the is the ratio of specific heat at constant pressure to specific heat at constant volume, $\mu = m_{\mathrm{H}}$ is the mass per particle, v_s is the shock velocity, and k_B is the Boltzmann constant.

The ionization fractions were also calculated face by face, with a mass flux-weighted average determining the overall cell ionization fraction. Face contributions were calculated according to

$$\frac{n(\mathrm{A})}{n(\mathrm{A}^+)} = \frac{\langle\sigma v\rangle_{rr}}{\langle\sigma v\rangle_{ci}} = \frac{2^4}{3^{3/2}}(\frac{e^2}{\hbar c})^3\frac{B}{k_BT}e^{B/k_BT} \tag{2}$$

$$\chi_{\mathrm{H}+} = \frac{n(H+)}{n(H)+n(H+)} = \Big(1+\frac{n(H)}{n(H+)}\Big)^{-1} \tag{3}$$

where we've taken the ionization energy $B = (157{,}800\mathrm{K})k_B$ for Hydrogen, $n(A) = n(H)$ to be the number density of hydrogen, $n(A^+) = n(\mathrm{H}+)$ the be the number density of hydrogen ions, $\langle\sigma v\rangle_{rr}$ and $\langle\sigma v\rangle_{ci}$ as the radiative recombination and collisional ionization rates, respectively, e to be the electron charge, and h to be planck's constant,. A temperature floor of 300 K for ionization was set, such that for cell temperatures below this value the ionization fraction was taken to be zero.

With temperatures and ionization fractions calculated for each face of each cell, a single average value was determined for each cell by weighting each face f contribution by the flux from the corresponding neighboring cell n,

$$T = \frac{\sum_f T_f v_n \rho_n}{\sum_f v_n \rho_n} \tag{4}$$

$$\chi_{\mathrm{H}+} = \frac{\sum_f \chi_{\mathrm{H}+,f} v_n \rho_n}{\sum_f v_n \rho_n} \tag{5}$$

That is, for cell $(z, x, y) = (i, j, k)$, the value at the lower z face was weighted by the density and velocity at cell $i-1$, the value at the upper z face was weighted by the density and velocity at cell $i+1$, the left x value was weighted by the $j-1$ density and velocity, the x face by cell $j+1$, back y face by cell $k-1$, and front y face by cell $k+1$ temperature and ionization fraction contributions.

The shocks in our simulation were modeled adiabatically, and their resulting temperature and ionization fraction was assumed to fill the entire cell. These approximations are reasonable as long as the shocked gas fills the cell before significant cooling takes place. The cooling time can be found using the cooling function approximation for $T > 10^5$K,

$$\Lambda(T) \approx C\Big(\frac{T}{10^6\mathrm{K}}\Big)^{-0.7} n_{\mathrm{H}}n_{\mathrm{e}} \quad C = 1.1\times10^{-22}\mathrm{erg\ cm^3\ s^{-1}} \tag{6}$$

to get cooling time

$$t_{\mathrm{cool}} = \frac{(3/2)(n_{\mathrm{H}}V)(k_B\times\mathrm{K})(T/\mathrm{K})}{\Lambda(T)V} \approx \frac{(3/2)(k_B\times\mathrm{K})}{C\chi_{\mathrm{H}+}n_{\mathrm{H}}}\frac{(T/\mathrm{K})^{1.7}}{10^{4.2}} \tag{7}$$

and the approximation for $T < 10^5K$,

$$\Lambda \approx D(T/\mathrm{K})^{1.6}n_{\mathrm{H}}n_{\mathrm{e}} \quad D = 3.98\times10^{-30}\mathrm{erg\ cm^3\ s^{-1}} \tag{8}$$

to get cooling time

$$t_{\mathrm{cool}} = \frac{(3/2)(n_{\mathrm{H}}V)(k_B\times\mathrm{K})(T/\mathrm{K})}{\Lambda(T)V} \approx \frac{(3/2)(k_B\times\mathrm{K})(T/\mathrm{K})^{-.6}}{D\chi_{\mathrm{H}+}n_{\mathrm{H}}} \tag{9}$$

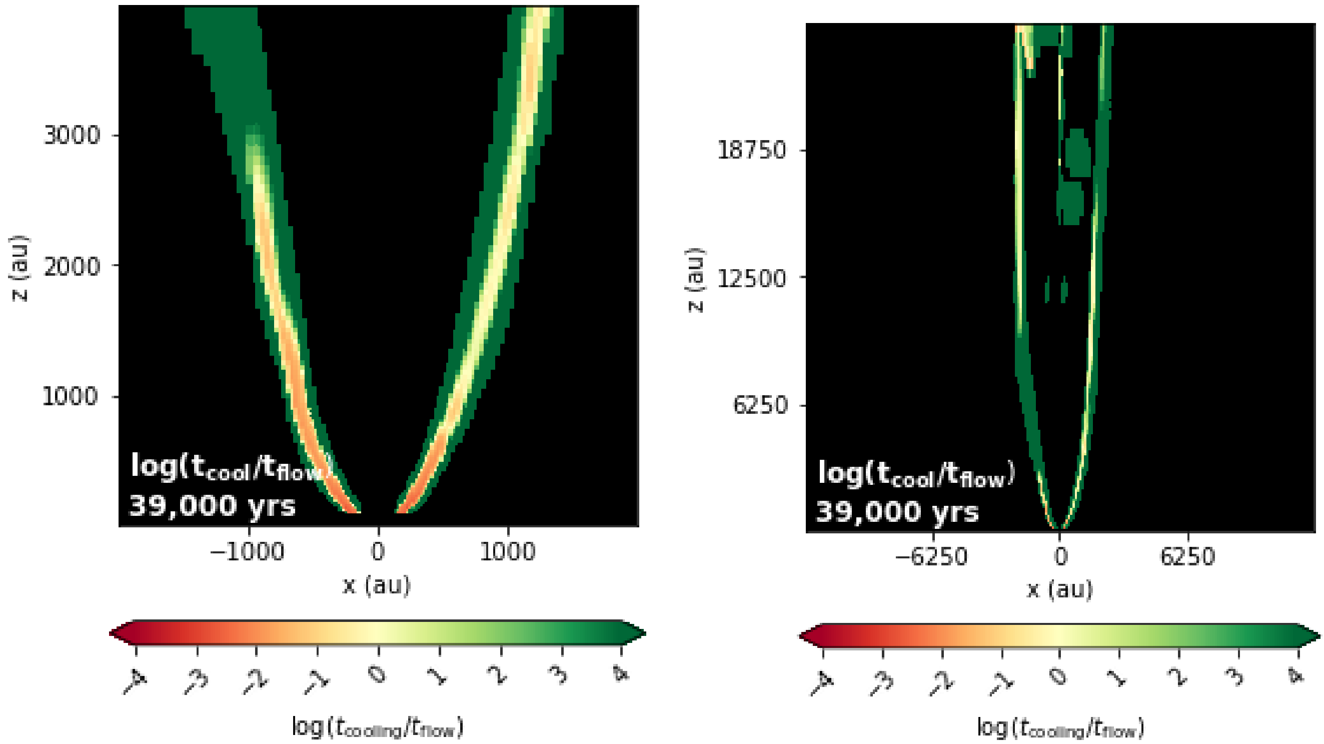

Figure 1. Ratio of timescales $t_{\rm cool}/t_{\rm flow}$ for the 39,000 yrs, $8M_\odot$ snapshot for the region $-2000 < x < 2000$, $0 < z < 4000$ on the left and for $-12500 < x < 12500$, $0 < z < 25000$ on the right. Diverging color scales show most of the region to have larger cooling times, with the exception of several highly-emitting regions.

These are compared to the flow time for the shocked gas to fill the cell, given as a mass-flux-weighted average of the converging shock's timescale from each face f,

$$t_{\rm flow} = \frac{\sum_{v_s>0} t_{{\rm flow},f} v_{\rm n}\rho_{\rm n}}{v_{\rm n}\rho_{\rm n}} = \frac{\sum_{v_s>0} |(\frac{1}{2}\Delta s)/(v_s/4)| v_{\rm n}\rho_{\rm n}}{v_{\rm n}\rho_{\rm n}} = 2\frac{\sum_{v_s>0} |\Delta s/v_s| v_{\rm n}\rho_{\rm n}}{v_{\rm n}\rho_{\rm n}} \tag{10}$$

where $v_s/4$ is the post-shock velocity and $\frac{1}{2}\Delta s$ is the distance from the edge to the center of the cell.

A map of the ratio $t_{\rm cool}/t_{\rm flow}$ is plotted for an example $8M_\odot$ snapshot in Fig. 1. This figure shows that there are significant regions with cooling times down to .01 times shorter than flow times. Thus, adjustments to the current intensity calculation methods will be made in future research to account for these cooling times. This will be done by scaling the depth of each cell integrated over in the 1D radiative transfer equation by the ratio of $t_{\rm cool}/t_{\rm flow}$ when this value is less than 1. The results in this paper are preliminary, and do not account for the cooling effects.

2.3. *Calculating Free-Free Radio Emission*

With the aforementioned flux-weighted temperature T and flux-weighted ionization fraction $\chi_{\rm H+}$, we calculate the variables dictating free-free radio emissions due to shocks in the simulated outflow. We find the emission coefficients j_ν, absorption coefficients κ_ν, and optical depths in each axial direction $\tau_{\nu,z}, \tau_{\nu,x}, \tau_{\nu,y}$ as follows:

$$j_\nu = 3.86 g_{\rm ff} \frac{e^6}{m_e^2 c^3} \left(\frac{m_e}{k_B T}\right)^{1/2} n_e n_p e^{-h\nu/(k_B T)} \ [\text{erg cm}^{-3}\ \text{sr}^{-1}\ \text{Hz}^{-1}\ \text{s}^{-1}] \tag{11}$$

$$\kappa_\nu = \frac{4}{3}\left(\frac{2\pi}{3}\right)^{1/2} \frac{n_e n_p e^6 g_{\rm ff}}{m_e^{3/2} c (kT)^{3/2}} \frac{1}{\nu^2} \ [\text{cm}^{-1}] \tag{12}$$

]

$$\tau_{\nu,z} = \kappa_\nu \Delta z, \quad \tau_{\nu,x} = \kappa_\nu \Delta x, \quad \tau_{\nu,y} = \kappa_\nu \Delta y, \tag{13}$$

using ion densities $n_e = n_p = n_{\mathrm{H}+} = (\chi_{\mathrm{H}+}\rho)/m_H$, hydrogen mass $m_H = (1.4)(1.67 \times 10^{-24})$ g, and gaunt factor $g_{\mathrm{ff}} = 5.96(T/10^4\mathrm{K})^{0.15}(\nu/\mathrm{GHz})^{-0.1}$. This was replicated for frequencies, ν of .01, .05, .1, .5, 1, 5.3, 23, 43, 100, and 230 GHz.

Specific intensity, I_ν was calculated along lines of sight for the x-z plane, y-z plane, and x-y plane by the 1D radiative transfer equation,

$$I_\nu(s) = I_\nu(0)e^{-\tau_\nu} + \int_0^s ds' j_{\mathrm{ff}} e^{-[\tau_\nu(s)-\tau_\nu(s')]} = I_\nu(0)e^{-\tau_\nu} + \int_0^{\tau_\nu} \left[\frac{j_{\mathrm{ff},\nu}}{\kappa_{\mathrm{ff},\nu}}\right] e^{-(\tau-\tau')} d\tau' \tag{14}$$

and discretized this equation for uniform temperature within each cell. Beginning with the emission intensity from the farthest cell, the absorption and emission were calculated for each cell, propagating forwards, to yield the intensity of the foremost frame of cells. The farthest cell emission, $I_{\nu,0}$, was given by

$$I_{\nu,0} = j_\nu * \Delta s \tag{15}$$

in which Δs is the length of the cell in the line of sight direction, (the y-direction for the x-z plane).

Then, to calculate the emission of the next cell, this value was used in

$$I_\nu = I_{\nu,0}e^{-\tau_{\nu,s}} + \left[\frac{j_{\mathrm{ff},\nu}}{\kappa_{\mathrm{ff},\nu}}\right](1 - e^{-\tau_{\nu,s}}) \tag{16}$$

which served as $I_{\nu,0}$ for the cell in front of it, and so on. Intensity maps of $I_\nu[\mathrm{mJy/as^2}] = \frac{I_\nu}{[\mathrm{erg\ cm^{-2}s^{-1}Hz^{-1}sr^{-1}}]}\frac{10^{26}}{4.2545\times10^{10}}$ were produced by conducting this calculation for every line-of-sight column.

Fluxes S_ν were predicted for x-z frame regions of $-r/2 < x < r/2$ and $0 < z < r$, for scales of $r = 1000$, 2000, 4000, 8000, 16000, and 32000 au. 32000 au represents the entirety of the simulation, which in reality only extends to ±15000 au in the x and y directions, and 25000 au in the z direction. These fluxes were calculated as a surface integral of the intensity over the solid angle region $\Omega = A/d^2$,

$$S_\nu \equiv \int I_\nu d\Omega = \sum_{i,j} I_{\nu,i,j}[\mathrm{mJy/as^2}]\frac{\Delta x_1 \Delta x_2}{r^2}(4.2545 \times 10^{10}\mathrm{as^2}) \tag{17}$$

at a distance of $d = 1$ kpc, then doubled to account for the opposite bipolar jet. In doing so for each frequency and snapshot, we obtained predicted spectra and fluxes for a given frequency over time.

Finally, we characterize the flux variability by considering higher frequency snapshots of 10 year intervals for each protostellar mass of interest, beginning with the earliest well-defined snapshots of 1.5M$_\odot$ at 4,000 years up to 24 M$_\odot$ at 93,000 years. The average 10 year variation over a period of 100 years is

$$\langle \Delta S_\nu / S_\nu \rangle = \frac{1}{N-1}\sum_{n=1}^{N-1} \frac{|\log(S_{\nu,n} - \log(S_{\nu,n+1}|}{S_{\nu,n}} \tag{18}$$

given by Eq. (x), in which snapshots n and $n+1$ are each 10 years apart and the number of snapshots (over this 100 year period) is $N = 11$.

2.4. *Single Cell Examples*

For an example of how the calculations were made, we consider a half-ionized example cell from the 39,000 year ($8M_\odot$) snapshot. The partially ionized cell is marked by indices $(i, j, k) = (156, 141, 139)$ defined such that z_array$[i] = z$, x_array$[j] = x$, and y_array$[k] = y$, and shown in fuchsia in Fig. **??**. The relevant simulation data for cell $(156, 141, 139)$ and each of it's neighboring cells are given in columns 1 through 9 of the top section of Table **??**, with extraneous neighboring cell data excluded. The velocity difference, shock velocity, shock temperature, and ionization fraction for each face f are then given in columns 10-13 of Table 1, calculated according to Eq.s (1)-(3). Averaging the face temperatures T_f and face ionization fractions $\chi_{\mathrm{H}+,f}$ by the mass-fluxes ρv_f according to Eq. (4) and Eq.(5), yielded flux-weighted average values of $T = 17,700$K and $\chi_{\mathrm{H}+} = .49$ for the cell.

Since this temperature is less than 10^5K, we insert $T = 17,700$K, $\chi_{\mathrm{H}+} = .49$, and $n_{\mathrm{H}} = \rho/m_{\mathrm{H}} = (1.68 \times 10^{-23}\mathrm{g/cm^3})/(2.34\mathrm{g}) = 7.17\mathrm{cm^{-3}}$ into Eq. (9), to find the cooling time, $t_{\mathrm{cool}} = 1326$yrs. For the flow time, we average the timescales from all sides with non-zero shock velocity, those being m1, p1, and m2. For this cell, $\Delta z = 7.24 \times 10^{10}$ km and $\Delta x = 1.84 \times 10^{9}$ km. Dividing $\frac{\Delta s}{2}$ by $\frac{v_s}{4}$ for each of these shocks gives time scales of 210 yrs, 137 yrs, and 614 yrs, respectively. The flux-weighted average of these values yields $t_{\rm flow} = 176$yrs. Thus, we find a ratio $t_{\rm cool}/t_{\rm flow} = 1326/176 \sim 7.5$, indicating that the cooling time is ~ 7.5 times the flow time, so it is reasonable in this case to assume the shock variables flood the cell before significant cooling occurs.

Cell $(i, j, k) = (7, 122, 139)$ serves as a counter example, where flow times exceed cooling times. The cell is marked in green in Fig. **??** and the relevant simulation data, velocity difference, shock velocity, shock temperature, and ionization fraction for each face are found in the middle section of Table 1. Averaging the T_f and $\chi_{\rm H+,f}$ values by the ρv_f values according to Eq. (4) and Eq.(5), yielded $T = 12,100$K and $\chi_{\rm H+} = .41$ for the cell. Since this temperature is less than 10^5K, we insert $T = 12,100$K, $\chi_{\rm H+} = .41$, and $n_{\rm H} = \rho/m_{\rm H} = (3.38 \times 10^{-19}{\rm g/cm^3})/(2.34{\rm g}) = 145,000{\rm cm^{-3}}$ into Eq. (9) to find $t_{\rm cool} = 0.098$yrs. To calculate flow time, we consider the sides with non-zero shock velocity which are now only m2, and p2, with cell width $\Delta s = \Delta x = 2.77 \times 10^{9}$ km. Dividing $\frac{\Delta s}{2}$ by $\frac{v_s}{4}$ for these two shocks gives time scales of 4.88 yrs and 4.87 yrs, respectively, with a flux-weighted average of $t_{\rm flow} \sim 4.9$yrs. The cooling to flow times ratio of $t_{\rm cool}/t_{\rm flow} = .02$ indicates that cooling occurs before the shock variables have flooded the cell.

Finally, We consider an especially hot, mostly (95%) ionized test cell with indices $(i, j, k) = (165, 191, 139)$. The cell is marked in yellow in Fig. **??** and the relevant simulation data, velocity difference, shock velocity, shock temperature, and ionization fraction for each face are found in the bottom section of Table 1. Averaging the T_f and $\chi_{\rm H+,f}$ values by the ρv_f values according to Eq. (4) and Eq.(5), yielded $T = 3,924,000$K and $\chi_{\rm H+} = .95$ for the cell. Since this temperature is greater than 10^5K, we insert $T = 3,924,000$K, $\chi_{\rm H+} = .95$, and $n_{\rm H} = \rho/m_{\rm H} = (3.94 \times 10^{-22}{\rm g/cm^3})/(2.34{\rm g}) = 168.6{\rm cm^{-3}}$ into Eq. (7), to find the cooling time, $t_{\rm cool} = 3807$yrs. The sides with non-zero shock velocity are now only m1, and p1, with cell height $\Delta s = \Delta z = 7.24 \times 10^{10}$ km. Dividing $\frac{\Delta s}{2}$ by $\frac{v_s}{4}$ for these two shocks gives time scales of 15.39 yrs and 12.35 yrs, respectively. A flux-weighted average then yields $t_{\rm flow} = 13.52$ years. Thus, we find a ratio $t_{\rm cool}/t_{\rm flow} = 3807/13.52 \sim 282$, indicating that the cooling time is ~ 282 times the flow time, so it is again reasonable in this case to assume the shock variables flood the cell before significant cooling occurs.

3. RESULTS

3.1. *Shock Modeling*

Snapshots from the simulation at masses of 1.5, 2, 4, 8, 12, 16, and 24 $M_\odot$ were selected for post-processing, after the simulation reached 5,000, 9,000, 21,000, 39,000, 54,000, 68,000, and 93,000 years, respectively (see Jan et al. 2021, in preparation, for details). The post-shock state of each snapshot is displayed in slices in Fig. 1 for the entire snapshot object, and Fig. 2 zoomed in to the innermost 4000 au. The density and z-velocity magnitude produced by the Zeus-MP simulation are displayed in the first and second columns respectively. The density slices in the first column display a low-density cavity in the central jet region, ?(np.min)? g/cm^3, while the surrounding regions reach densities of approximately ?(np.max)? g/cm^3. This cavity increases in opening angle as it evolves from 8, to 12, to 16, to 24 $M_\odot$. The z-velocities exceed 1000 km/s in the jet cavity, whereas they remain low in the surrounding regions. At 12, 16, and 24 $M_\odot$, a region of 1-10 km/s surrounds the high-velocity jet region.

The third column shows the flux-weighted post-shock temperature, calculated as described in section 2.2. Temperatures are highest, reaching 10 million K on the boundary between the low-density, high-velocity jet and the surrounding higher density-low velocity envelope. One can deduce that this indicates shocks resulting from the high velocity gradient at this interface. The fourth column shows these high temperature regions to be nearly entirely ionized due to shocks. Finally in the fifth column the 5.3GHz emissivities are shown, peaking in at the jet-envelope interface around ?? 10E-4 - check code?? mJy/cm. The ionization fraction and emissivity slices demonstrate a gap in shocks near ~1000-5000 au in the snapshots up to 39,000 years.

3.2. *Ionization Fractions*

Averaged Jet Ionization Fractions—Predicted ionization fractions of the jet are one parameter by which the results of our simulation are comparable to observations. Thus, several processes to calculate an observable ionization fraction, that being a projected line-of-sight average, were considered. The jet was defined as including any cell with $v_z > v_{\rm min}$, for $v_{\rm min} = 10$, 100, and 1000 km s^{-1}. To create a 2D projection, we averaged the ionization fractions over the line-of-sight y-column in three ways: (1) mass-weighted, (2) volume-weighted, (3) emissivity-weighted, as follows:.

Table 1. Test Cell Simulation Data

f	(i,j,k)	z	x	y	ρ	v_z	v_x	v_y	$v_f - v_{\rm cur}$	v_s	T_f	$\chi_{{\rm H}+,f}$	ρv_f
(face)		[au]	[au]	[au]	[g/cm^3]	[km/s]	[km/s]	[km/s]	[km/s]	[km/s]	[K]		[g/cm^3 km/s]
cur	(156,141,139)	20008	18	-6	1.68E-23	1316.82	2.86	-0.45					
m1	(155,141,139)	19530	18	-6	1.69E-23	1338.65			21.83	21.83	10804	0.025	3.68E-22
p1	(157,141,139)	20498	18	-6	1.62E-23	1283.43			-33.39	33.39	25276	0.996	5.42E-22
m2	(156,140,139)	20008	6	-6	1.20E-23		1.05		-1.81	0	0	0	0.00
p2	(156,142,139)	20008	30	-6	2.18E-23		2.67		-0.19	0.19	1	0	4.14E-24
m3	(156,141,138)	20008	18	-18	1.87E-23			-1.25	-0.8	0	0	0	0
p3	(156,141,140)	20008	18	6	1.99E-23			0.32	0.77	0	0	0	0
cur	(165,191,139)	24860	1261	-6	3.94E-22	821.22	66.03	-0.03					
m1	(164,191,139)	24268	1261	-6	3.62E-22	1190.02			368.80	368.8	3083619	1.000	1.34E-19
p1	(166,191,139)	25465	1261	-6	1.90E-21	361.52			-459.70	459.7	4791019	1.000	8.75E-19
m2	(165,190,139)	24860	1217	-6	3.11E-22		64.51		-1.52	0	0	0	0
p2	(165,192,139)	24860	1305	-6	5.85E-22		67.01		0.98	0	0	0	0
m3	(165,191,138)	24860	1261	-18	3.89E-22			-0.93	-0.90	0	0	0	0
p3	(165,191,140)	24860	1261	6	4.16E-22			0.53	0.56	0	0	0	0
cur	(7,122,139)	195	-261	-6	3.39E-19	130.98	-96.36	-5.93				0	
m1	(6,122,139)	181	-261	-6	4.31E-19	101.4			-29.58	0	0	0	0
p1	(8,122,139)	210	-261	-6	2.79E-19	161.48			30.50	0	0	0	0
m2	(7,121,139)	195	-280	-6	4.77E-19		-60.44		35.92	35.92	29252	0.999	1.71E-17
p2	(7,123,139)	195	-243	-6	2.75E-19		-132.35		-35.99	35.99	29366	0.999	9.90E-18
m3	(7,122,138)	195	-261	-18	3.22E-19			-11.79	-5.86	0	0	0	0
p3	(7,122,140)	195	-261	6	3.75E-19			0.51	6.44	0	0	0	0

$$\langle \chi_{\rm H+} \rangle_{\rm mass} = \frac{\sum_k \chi_{i,j,k} \rho_{\nu,i,j,k} \Delta y_k}{\sum_k \rho_{\nu,i,j,k} \Delta y_k} \tag{19}$$

$$\langle \chi_{\rm H+} \rangle_{\rm vol} = \frac{\sum_k \chi_{i,j,k} \Delta y_k}{\sum_k \Delta y_k} \tag{20}$$

$$\langle \chi_{\rm H+} \rangle_{\rm emis} = \frac{\sum_k \chi_{i,j,k} j_{\nu,i,j,k} \Delta y_k}{\sum_k j_{\nu,i,j,k} \Delta y_k} \tag{21}$$

This was done across every y-column to produce the 2D ionization fraction maps shown in Figures 3 and 4. In both, mass, volume, and emission-weighting produce the results in the first three columns, middle three columns, and last three columns, respectively, Velocity cutoffs of 1, 10, and 100 km/s were applied in columns 1,4,7; columns 2,5,8; and columns 3,6,9, respectively. Time and mass increase from top to bottom, following the simulation as it grown from 2 to 24 $M_\odot$ at 9,000 to 93,000 years. Contour lines display these velocity cutoffs of the outflow, which evidently restrict the region of non-zero ionization fraction. Higher velocity cutoffs provided generally higher ionization fractions because they excluded slower-moving, less ionized gas, particularly on the outskirts of the jet. Emission-weighting provided the highest and most binary ionization fractions because, with ionization fraction and emissivity both dependent on shock temperatures, high emissivity correlated to high ionization fraction and vice versa.

Average ionization fractions of the jet were calculated by mass, volume, and emission weighting. The jet was defined to include all cells with $v_z \geq v_{\rm cutoff}$ for $v_{\rm cutoff}$ =1, 10, and 100 km/s. The quantitative results of Fig.s 3 and 4 are summed up quantitatively by their corresponding 3-dimensional averages in Table 2.

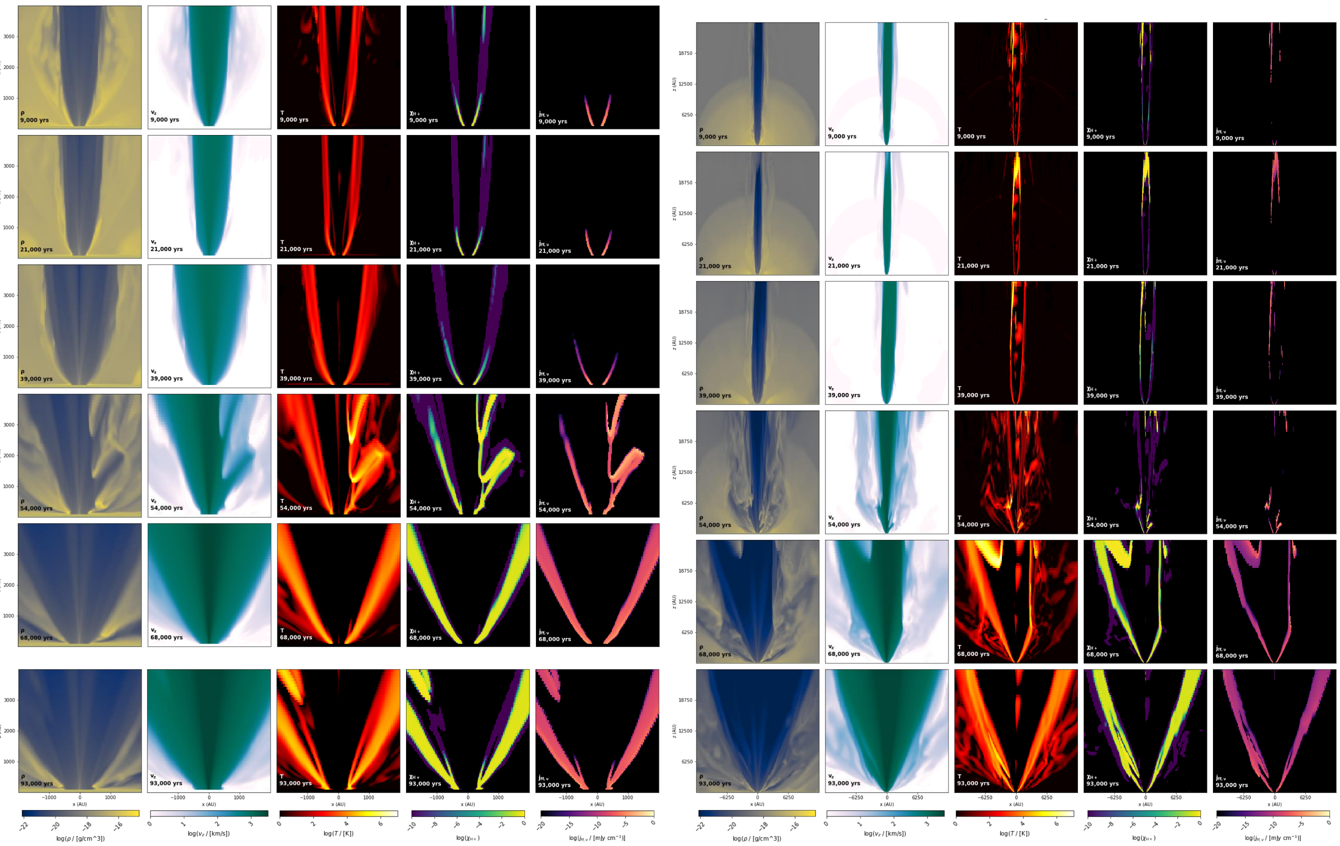

Figure 2. Time evolution of shock modeling variables in slices through the center of the simulation in the x-z plane, over the ranges (*left panel*) $-2000\text{au} < x < 2000\text{au}$, $0\text{au} < z < 4000\text{au}$ and (*right panel*) $-12500\text{au} < x < 12500\text{au}$, $0\text{au} < z < 25000\text{au}$. From left to right, the columns display density, velocity in the z-direction, temperature, ionization fraction, and emissivity. From top to bottom, the simulation grows in mass, reaching 2, 4, 8, 12, 16, 24 $M_\odot$ at 9,000, 21,000, 39,000, 54,000, 68,000, and 94,000 years, respectively.

Table 2. Averages Ionization Fractions of 2D Maps

Scale	Time	Mass-Weighted			Volume-Weighted			Emission-Weighted		
[au]	[yrs]	$\geq$1 km/s	$\geq$10 km/s	$\geq$100 km/s	$\geq$1 km/s	$\geq$10 km/s	$\geq$100 km/s	$\geq$1 km/s	$\geq$10 km/s	$\geq$100 km/s
	9,000 yrs	0.0085	0.0347	0.1228	0.0002	0.0003	0.0004	0.2179	0.2179	0.1630
	21,000 yrs	0.0109	0.0441	0.1030	0.0001	0.0001	0.0001	0.2317	0.2317	0.1608
4000	39,000 yrs	0.0203	0.0466	0.1173	0.0002	0.0002	0.0003	0.2783	0.2783	0.2028
	54,000 yrs	0.0064	0.0331	0.1368	0.0036	0.0052	0.0070	0.2872	0.2919	0.2838
	68,000 yrs	0.0119	0.0516	0.2001	0.0138	0.0173	0.0201	0.2761	0.2784	0.2856
	93,000 yrs	0.0149	0.0482	0.2470	0.0095	0.0153	0.0269	0.5353	0.5364	0.6666
	9,000 yrs	0.0996	0.1661	0.5137	0.0068	0.0084	0.0126	0.7003	0.7003	0.8509
	21,000 yrs	0.0202	0.1172	0.4097	0.0038	0.0070	0.0102	0.7996	0.7996	0.8396
25000	39,000 yrs	0.0198	0.1185	0.4742	0.0056	0.0117	0.0201	0.6983	0.6983	0.8345
	54,000 yrs	0.0134	0.0899	0.3538	0.0126	0.0200	0.0264	0.5645	0.5647	0.7733
	68,000 yrs	0.0132	0.1129	0.2740	0.0267	0.0387	0.0480	0.5222	0.5224	0.3991
	93,000 yrs	0.0059	0.0373	0.1762	0.0127	0.0233	0.0349	0.5374	0.5391	0.6510

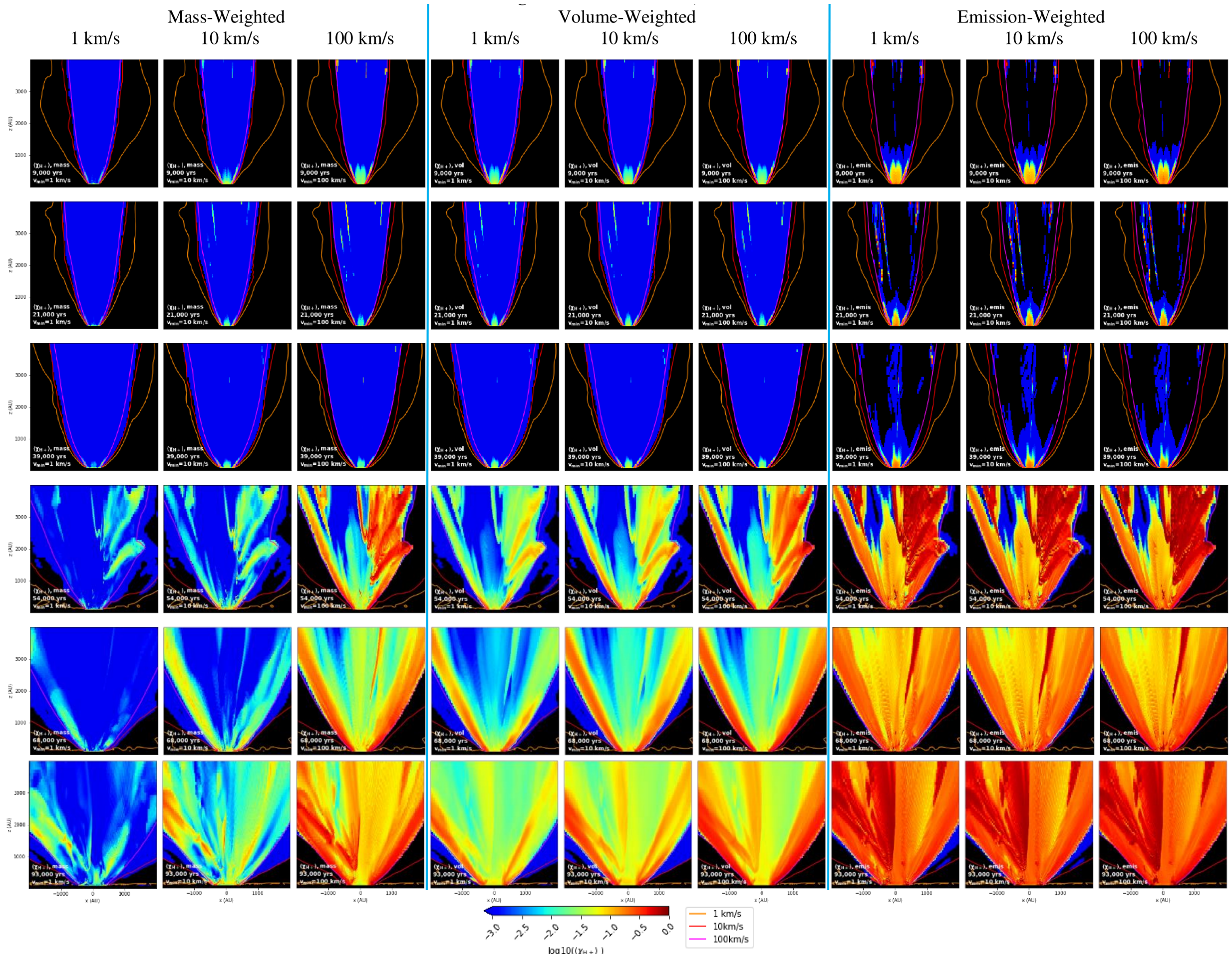

Figure 3. Average ionization fractions weighted by mass (*first three columns*), volume (*middle three columns*), and emission (*last three columns*). The average was calculated over all cells in the y-column that exceed cutoff velocities of $v_z \geq 1$ km/s (*columns 1, 4, 7*), 10 km/s (*columns 2, 5, 8*), and 100 km/s (*columns 3, 6, 9*), plotted over $-2000\text{au} < x < 2000\text{au}$, $0\text{au} < z < 4000\text{au}$. From top to bottom, the simulation grows in mass, reaching 2, 4, 8, 12, 16, 24 $M_\odot$ at 9,000, 21,000, 39,000, 54,000, 68,000, and 94,000 years, respectively. Contours are overlaid displaying where the maximum z-velocity along the projection meets the cutoffs of 1 km/s (*orange*), 10 km/s (*red*), and 100 km/s (*pink*).

To track the ionization fraction as a function of height above the midplane, the same averaging techniques were applied to slices of 1000 au along the z direction. Eqn.s (19)-(21) were modified to integrate over the 3-dimensional region as follows:

$$\langle \chi_{\mathrm{H}+,i,j} \rangle_{\mathrm{mass}} = \frac{\sum_{i,j,k} \chi_{i,j,k} \rho_{\nu,i,j,k} \Delta z_i \Delta x_j \Delta y_k}{\sum_{i,j,k} \rho_{\nu,i,j,k} \Delta z_i \Delta x_j \Delta y_k} \tag{22}$$

$$\langle \chi_{\mathrm{H}+,i,j} \rangle_{\mathrm{vol}} = \frac{\sum_{i,j,k} \chi_{i,j,k} \Delta z_i \Delta x_j \Delta y_k}{\sum_{i,j,k} \Delta z_i \Delta x_j \Delta y_k} \tag{23}$$

$$\langle \chi_{\mathrm{H}+,i,j} \rangle_{\mathrm{emis}} = \frac{\sum_{i,j,k} \chi_{i,j,k} j_{\nu,i,j,k} \Delta z_i \Delta x_j \Delta y_k}{\sum_{i,j,k} j_{\nu,i,j,k} \Delta z_i \Delta x_j \Delta y_k} \tag{24}$$

These resulted in the plots for each snapshot in Fig. 5. Again, emission-weighting provided the highest ionization fractions showing emitting regions to be almost entirely ionized, with dips near 2000-4000 au corresponding to the lack of shock-emissions in this region evident in the emissivity column of Fig. 2. Higher velocity cutoffs corresponded to higher ionization fractions, most noticeably in the mass-weighted case, attributable to the fact that the regions of slower moving gas (1-10 km/s) on the outskirts of the outflow were denser than the fast-moving jet cavity. Ionization fractions of four knots in the outflow of massive protostar G35.2-0.74N (Fedriani et al. 2019), are plotted alongside

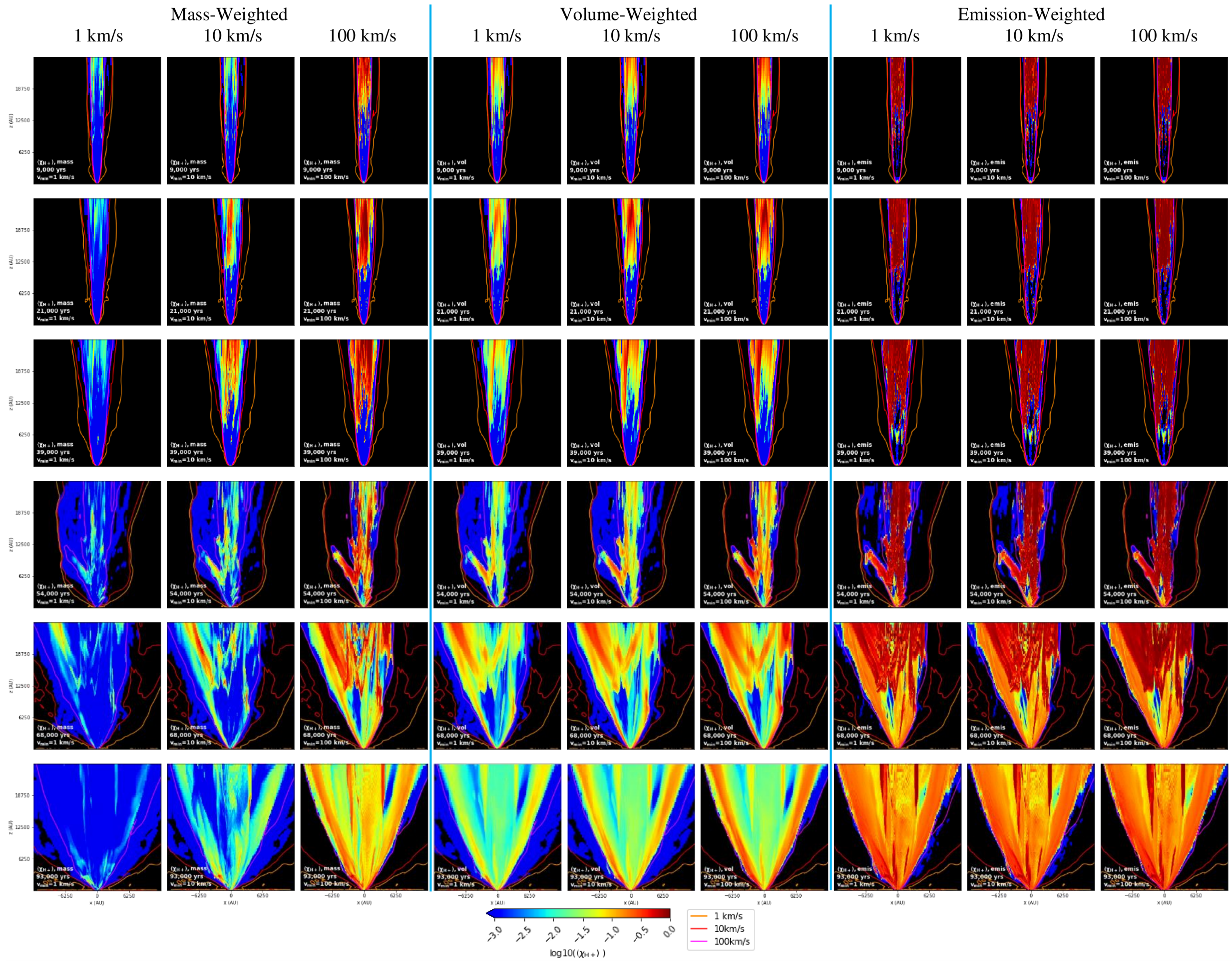

Figure 4. Same as Fig. 3, but for $-12500\text{au} < x < 12500\text{au}$, $0\text{au} < z < 25000\text{au}$.

the simulation-predicted values. Fedriani et. al's observed ionization fractions of 5-12% Fedriani et al. (2019) fall are within the range of predicted values.

3.3. *Radio Emissions*

3.3.1. *Intensity Mapping*

The intensities at radio frequencies of 0.05, 0.1, 0.5, 1, 5.3, 23, 43, 100, and 230 GHz were predicted and mapped, as shown for the 54,000 yrs $12M_\odot$ example in Fig. 3. The morphology appears similar at each frequency. However, it is dimmest at .01 GHz, brightens significantly up to 0.5 GHz, then maintains similar brightness up to 230 GHz. A quantitative analysis of flux vs. frequency is provided in section 3.3.4. We consider also the time evolution of these intensity maps at several scales. Fig. 7 illustrates this time evolution of the 5.3GHz and 230GHz intensity for the inner 1000 au region and entire 25000 au, along with mass-weighted, $v_{\rm cutoff} = 100\text{km/s}$ ionization fraction projections and ionized mass-weighted temperature projections. The most shock-ionized regions show average temperatures of 10 million K. In agreement with the low-shock region of $\sim$1000-5000 au indicated in the slice plots of Fig. 2 for snapshots up to 39,000 years, Fig. 7 shows this region to have average ionization fractions below .001%, average ionized-gas temperatures below #, and a gap in radio emissions.

A profile of the 5.3 and 230 GHz radio emissions as a function of height is given by integrating the flux over slices of 1000 au in the z-direction, as shown in Fig. 8. These profiles shows a drop in radio emissions below 10E-5 mJy for slices between 2000-8000 au, 1000-4000 au, and 1000-2000 au, for snapshots at 9,000, 21,000, and 39,000 years, respectively. For all snapshots except that of 54,000 years, the emissions are near constant from 10,000-25000 au.

3.3.2. *Integrated Flux*

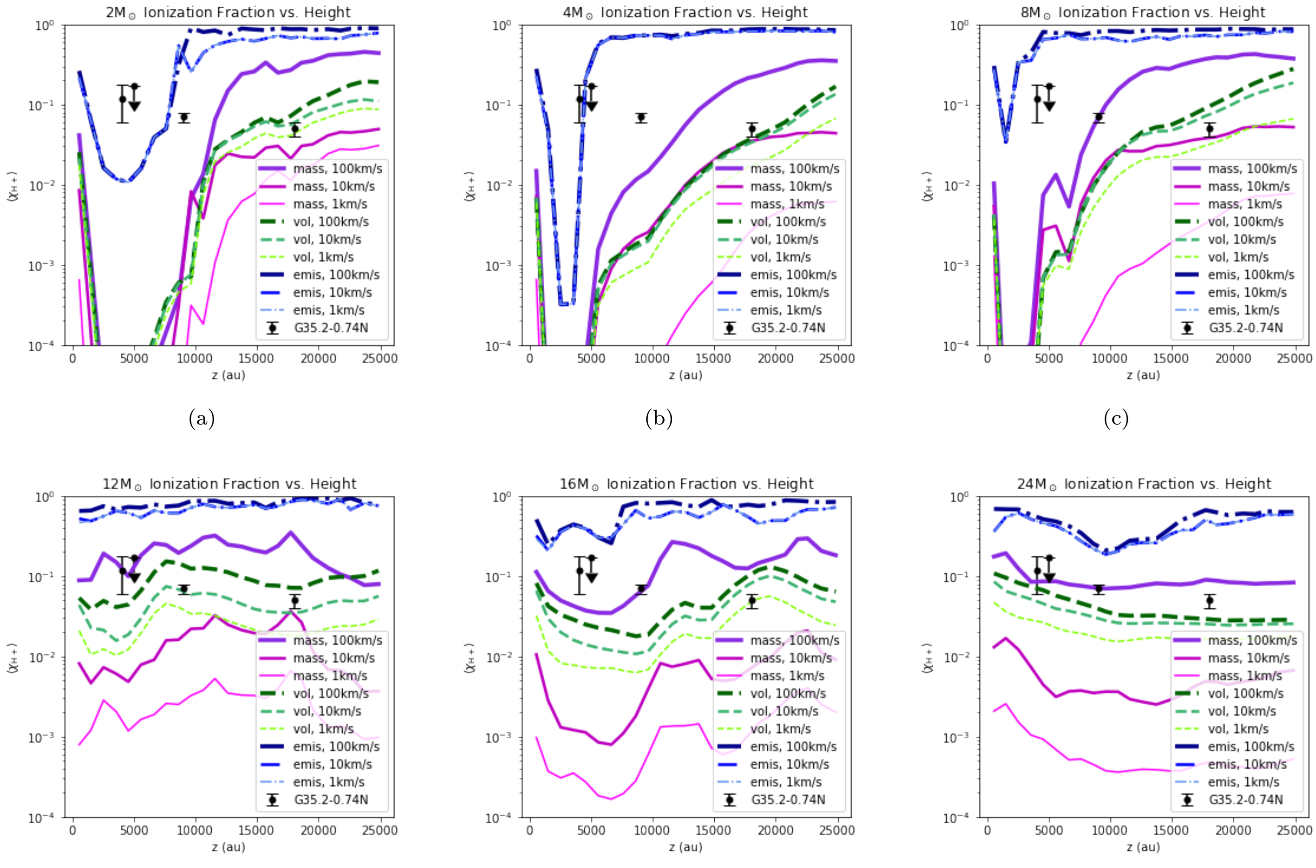

Figure 5. Average ionization fractions vs. height for 2, 4, 8, 12, 16, and 24 $M_\odot$ snapshots at 9,000, 21,000, 39,000, 54,000, 68,000, and 94,000 years are shown in (a), (b), (c), (d), (e), and (f), respectively. The ionization fractions were averaged by mass (*solid pinks*), volume (*dashed greens*), and emission (*dash-dotted blues*) over all cells in 1000au slices along the z-direction that exceed the cutoff velocities of $v_z \geq 100$ km/s (*thick*), 10 km/s (*medium*), and 1 km/s (*thin*). Overlaid are the ionization fractions calculated at 4 knots in massive star formation region G35.2-0.74N ((Fedriani et al. 2019).

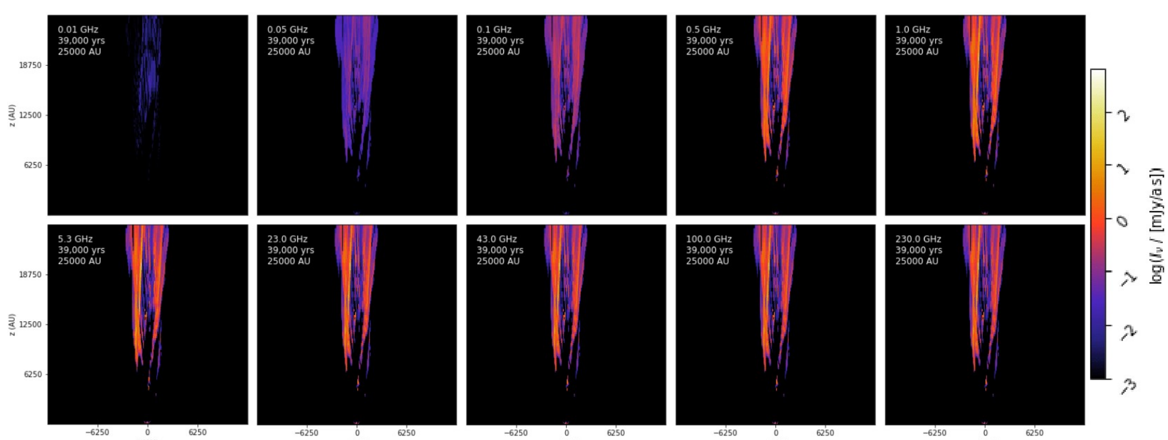

Figure 6. Intensity maps of 8M$_\odot$, 39,000 years snapshot at .01, .05, .1, .5, 1, 5.3, 23, 43, 100, and 230 GHz, over the range $-12500\text{au} < x < 12500\text{au}$, $0\text{au} < z < 25000\text{au}$.

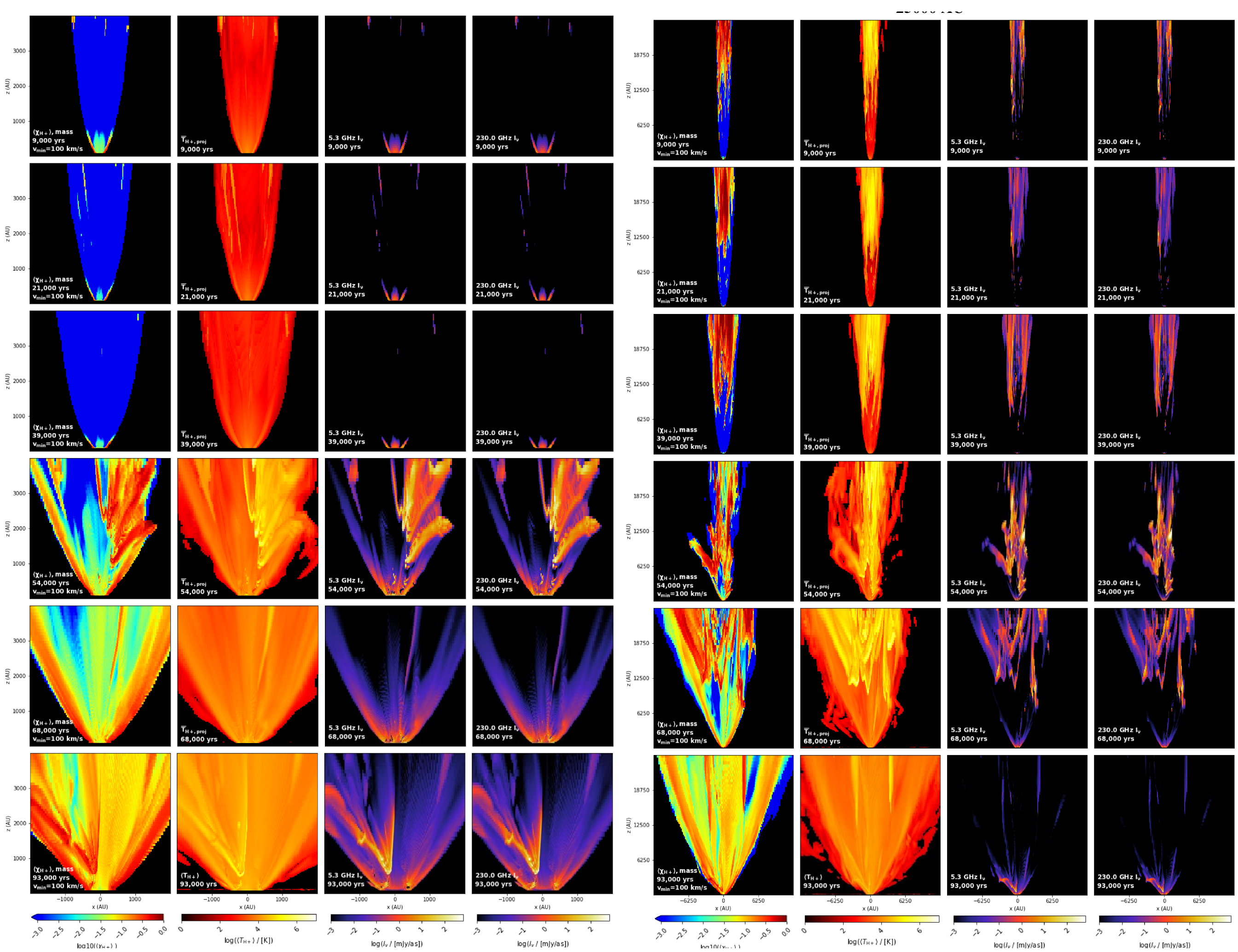

Figure 7. Time evolution of shock modeling variables projected along the y-direction. *Left:* ranges of over ($-2000\text{au} < x < 2000\text{au}$, $0\text{au} < z < 4000\text{au}$), and ($-12500\text{au} < x < 12500\text{au}$. *Right:* ranges over $0\text{au} < z < 25000\text{au}$), respectively. From left to right, the columns in each panel show mass-weighted average ionization fraction of the jet with a velocity cutoff of 100km/s, ionized-mass-weighted temperature, 5.3 GHz intensity, and 230 GHz intensityy each on a log scales.

A single integrated flux value at 5.3 GHz and 230GHz was calculated for every snapshot at scales of r = 500, 1000, 2000, 4000, 8000, 16000, and 32000 au, with the 100-year averages and standard deviations given in Table 3. The time evolution of these fluxes is plotted in Fig. 9, for scales of 1000, 2000, 4000, 8000, 16000, and 32000 au. Note, r=32000 au actually represents $-15000\text{au} < x < 15000\text{au}$, $0\text{au} < z < 25000\text{au}$, the entire range simulation range. The inner 1000 au region demonstrate an increase in flux over time, consistent with qualitative analysis of the intensity maps in Fig. 7, whereas the 4000-32000 au scales all dip at 21000 years ($4M_\odot$) and peak at 54000 years (12 $M_\odot$).

3.3.3. *Flux Variability*

The variability between snapshots every 10 years was also calculated for each snapshot mass. The average percent variation between consecutive snapshots, at each mass, is given as a function of time in Fig. 10. This average 10-year variability ranged from $\sim 2-20\% fortheinner 1000 auregion, andrangedfrom \sim 2-80\% fortheentiresnapshot, bothvaryingsignificantlybetweendifferentmasses.$

The 12 $M\odot$ set of snapshots, from 54,000-54,100 years is given as a case study of this flux variability, with the 5.3 and 230 GHz flux of each snapshot vs. time given in Fig. 11. This plot shows little change in either frequency's flux on the 4000-32000 au scales. However there is more variation evident in the inner 1000 and 2000 au regions between 54,050 to 54,090 years, with the corresponding 230GHz intensity maps shown in Fig. 12. The 2000 au scale flux

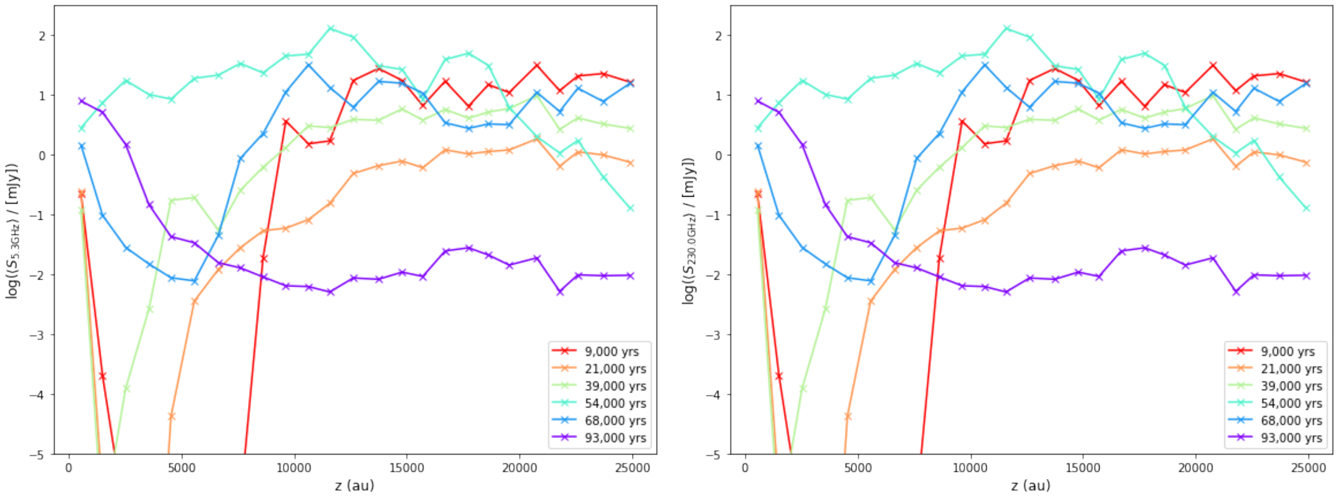

Figure 8. Flux at 5.3 GHz (*left*) and 230 GHz (*right*) vs. height, with fluxes calculated by integrating y-directed intensity I_ν over 1000au strips covering $-25000\text{au} < x < 25000\text{au}$, $h - 500\text{au} < z < h + 500\text{au}$ for each height h.

Table 3. Flux Data

Mass	Time	Lst	Log(Flux/[mJy])						
$[M_\odot]$	[yrs]	$[L_\odot]$	500au	1000au	2000au	4000au	8000au	16000au	32000au [a]
					5.3GHz				
1.5	5,000	896.89	-0.751 ± 0.006	-0.750 ± 0.006	-0.750 ± 0.006	0.793 ± 0.065	1.199 ± 0.060	2.185 ± 0.052	2.420 ± 0.021
2	9,000	1317.53	-0.652 ± 0.004	-0.649 ± 0.004	-0.649 ± 0.004	-0.474 ± 0.100	0.170 ± 0.087	1.904 ± 0.043	2.386 ± 0.019
4	21,000	1317.53	-0.666 ± 0.003	-0.665 ± 0.003	-0.665 ± 0.003	-0.614 ± 0.005	-0.012 ± 0.019	1.115 ± 0.080	1.367 ± 0.045
8	39,000	12499.00	-0.613 ± 0.002	-0.613 ± 0.002	-0.613 ± 0.002	-0.592 ± 0.011	0.442 ± 0.144	1.695 ± 0.049	2.147 ± 0.023
12	54,000	44323.60	0.332 ± 0.077	0.492 ± 0.098	1.037 ± 0.240	1.828 ± 0.061	2.382 ± 0.029	3.023 ± 0.023	3.158 ± 0.018
16	68,000	65461.50	0.439 ± 0.077	0.541 ± 0.077	0.561 ± 0.073	0.578 ± 0.075	0.641 ± 0.060	2.348 ± 0.010	2.579 ± 0.011
24	93000	84459.80	0.508 ± 0.072	1.009 ± 0.255	1.457 ± 0.034	1.549 ± 0.038	1.565 ± 0.043	1.567 ± 0.043	1.571 ± 0.042
					230 GHz				
1.5	5000	896.89	-0.909 ± 0.006	-0.909 ± 0.006	-0.909 ± 0.006	0.699 ± 0.097	1.103 ± 0.076	2.131 ± 0.068	2.328 ± 0.033
2	9000	1317.53	-0.811 ± 0.004	-0.808 ± 0.004	-0.808 ± 0.004	-0.631 ± 0.104	0.021 ± 0.087	1.809 ± 0.059	2.263 ± 0.021
4	21000	1317.53	-0.820 ± 0.003	-0.820 ± 0.003	-0.819 ± 0.003	-0.770 ± 0.005	-0.173 ± 0.019	0.958 ± 0.082	1.207 ± 0.046
8	39000	12499.00	-0.770 ± 0.002	-0.770 ± 0.002	-0.770 ± 0.002	-0.748 ± 0.011	0.291 ± 0.151	1.541 ± 0.053	1.990 ± 0.025
12	54000	44323.60	0.526 ± 0.282	0.660 ± 0.223	1.107 ± 0.193	1.793 ± 0.061	2.353 ± 0.034	3.151 ± 0.044	3.238 ± 0.029
16	68000	65461.50	0.788 ± 0.237	0.828 ± 0.218	0.837 ± 0.213	0.843 ± 0.211	0.872 ± 0.194	2.242 ± 0.018	2.457 ± 0.016
24	93000	84459.80	0.650 ± 0.145	1.262 ± 0.408	1.670 ± 0.076	1.713 ± 0.072	1.720 ± 0.072	1.721 ± 0.072	1.723 ± 0.072

NOTE—5.3GHz Fluxes in the +y direction integrated over $-r/2 < x < r$, $0 < z < r$ for each scale r = 500, 1000, 2000, 4000, 8000, 16000, and 32000 au.

[a] 32000 au spans the entire simulation, which actually only extends to $-15000\text{au} < x < 1500\text{au}$, $0\text{au} < z <$ au.

decreases during the last 50 years, most notably for the 230GHz flux from 16.70 mJy at 54,050 years to 4.61 mJy at 54,090 years. This can be attributed the movement of the bright feature displayed in the 2000au plots in Fig. 12 out of the scale's range. At 230GHz, there was also a significant brightening in the 1000 au flux, peaking at 12.08 mJy at 54,070 years, as a dense knot from the outer injection sight was exposed to the low-density outflow channel. This produce increased shock-heating in a handful of cells and brightening in the projected location $x = 18.15$au, $z = 141.83$au, visible in the 500 au scale of Fig. 12.

3.3.4. *Spectra*

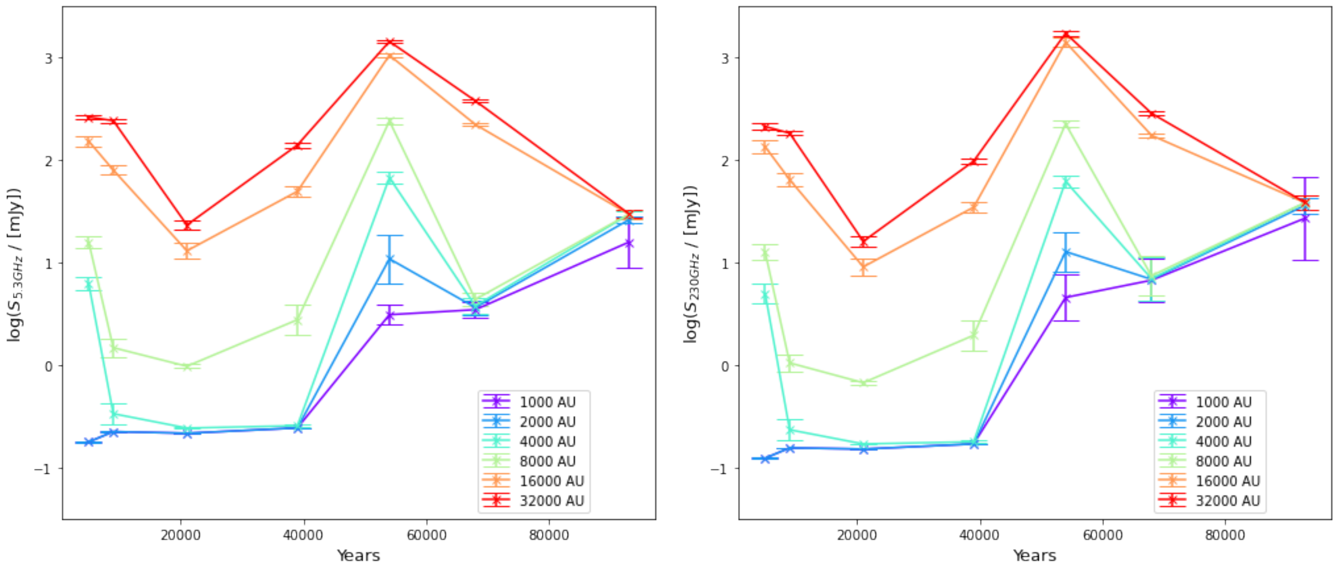

Figure 9. Average 5.3 GHz (*left*) and 230 GHz (*right*) flux over time for each snapshot (5,000, 9,000, 21,000, 39,000, 54,000, 68,000, and 94,000 years), integrated over regions of $-r/2 < x < r/2$, $0 < z < r$ for $r = 1000$, 2000, 4000, 8000, 16000, and 32000 au in purple, blue, turquoise, green, orange, and red, respectively. The fluxes were plotted as geometric means of the fluxes every 10 years for the 100 years following each snapshot, with error bars given by the standard deviation of the log-space flux averages. These values are given in Table 2.

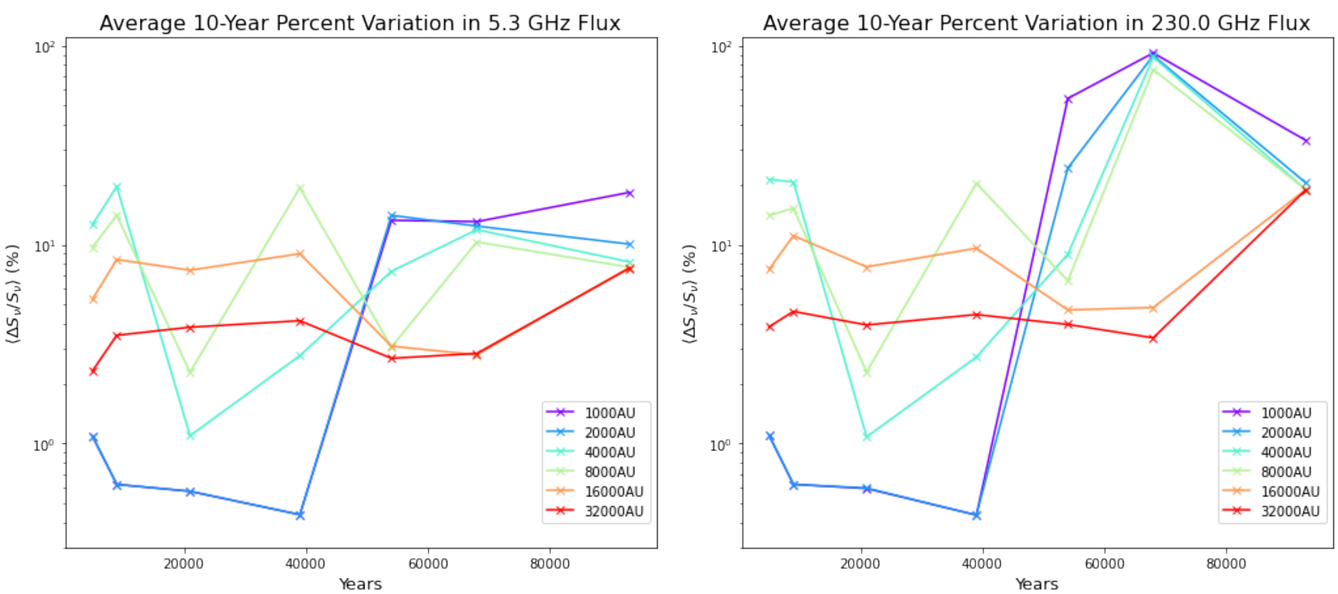

Figure 10. Average 10-Year percent variation in 5.3 GHz (*left*) and 230 GHz (*right*) flux $\langle \Delta S_\nu / S_\nu \rangle$ over 100 years vs snapshot times of 5,000, 9,000, 21,000, 39,000, 54,000, 68,000, and 94,000 years, calculated by Eq. 18.

To observe the time evolution of the spectra, the fluxes of each snapshot were plotted vs. their frequencies. The spectra from the inner 1000 au region and the entire snapshot are plotted in Fig. **??**. Their power-law shape is fairly consistent over time for the inner 1000 au region, demonstrating a slope approaching 2 at low frequencies and -.1 at high frequencies, whereas the spectral evolution of the entire snapshot region demonstrates more variability. As identified in the 5.3 and 230 GHz flux over time predictions of Fig. 9 the 54000 years ($12 M_\odot$) snapshot was brighter than the rest at high frequencies, exceeding by $\sim$1 order of magnitude.

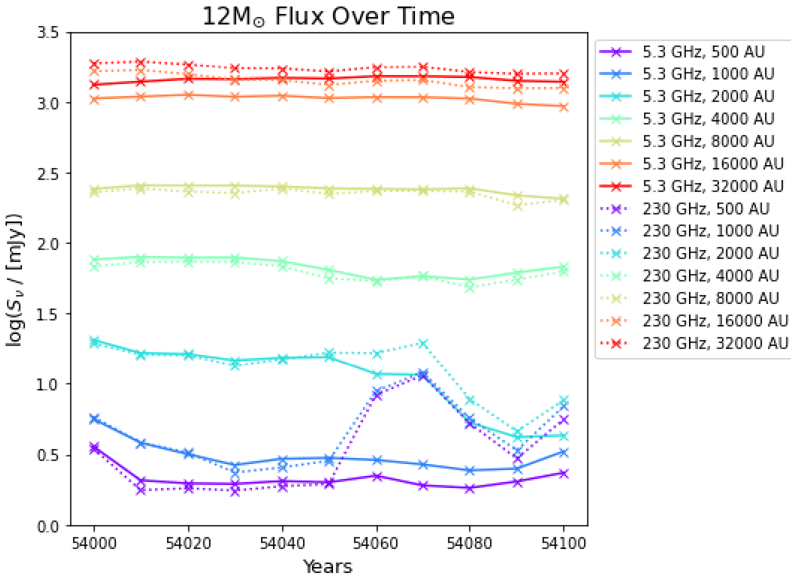

Figure 11. 5.3 GHz (*solid lines*) and 230 GHz (*dotted lines*) flux over time for the 12M$_\odot$, 54,000 years snapshot, in 10-year intervals. The 5.3GHz remains fairly constant for every scale over the 100 years, and the 230GHz flux remains fairly constant for scales of 4000-32000 au over the 100 years. The 2000 au 230GHz flux decreases from 16.70 mJy at 54,050 years to 4.61 mJy at 54,090 years. The 500au and 1000au 230GHz fluxes both peak at 54,070 years, at 11.47 mJy and 12.08 mJy, respectively.

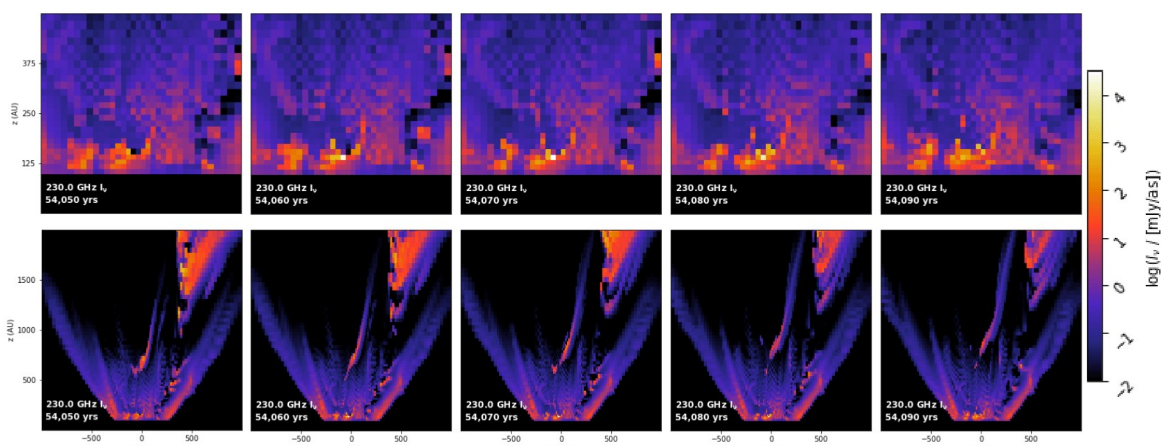

Figure 12. 230 GHz Intensity for 12M$_\odot$ snapshots between 54,050-54,090 years, over the range $-250 < x < 250,\ 0 < z < 500$ au (top) and $-1000 < x < 1000,\ 0 < z < 2000$ au (bottom). The intensity reaches peak value 29,299 mJy/as at 54,070 years, $x = $18.15 au, $z = $141.83, when a dense knot from the outer injection sight got exposed to the low-density outflow channel. The bright feature near $x \sim$500au, $z \sim$1750au moves upwards such that much of it exceeds $z = $ 2000au, causing the intensity in the 2000 au region to decrease over this 40 year span.

For a quantitative comparison of spectral indices to optically thin and thick limit expectations, Table 4 gives the slope between points for each pair of consecutive frequency points in the plots. The low frequencies represent the optically thick case, where the spectral index is expected to approach 2, whereas the high frequencies represent the optically thin limit, where the spectral index is expected to approach -.1. Comparing the slope between .01-.05 GHz points to the optically thick expectation, the inner 1000 au region offered a near match with slopes increasingly slightly over time, but ranging between 1.9-2.2. The entire snapshot showed a decrease in low-frequency slope over time, from 1.9, 1.1, notably lower than the optically thick expectation of 2. Comparing the slope between 100-230 Ghz points to the optically thin expectation, both scales provided a near match to the expected -.1 for their first 54,000 years, but

Table 4. Spectral Indices

Scale [au]	Snapshot [yrs]	.01-.05GHz	.05-.1GHz	.1-.5GHz	.5-1GHz	1-5.3GHz	5.3-23GHz	23-43GHz	43-1000GHz	100-230GHz
	5,000	1.9372	1.8895	1.5758	0.8523	0.119	-0.0904	-0.0995	-0.1005	-0.1015
	9,000	1.9444	1.8325	1.5094	0.7824	0.1028	-0.0911	-0.0995	-0.1004	-0.1014
	21,000	1.9227	1.7938	1.557	1.0276	0.2253	-0.0839	-0.0989	-0.1003	-0.1013
1,000	39,000	1.8395	1.8117	1.6399	1.0086	0.1764	-0.0878	-0.0992	-0.1002	-0.101
	54,000	2.1925	2.0825	1.5315	1.0262	0.7056	0.14	-0.0365	-0.0811	-0.0973
	68,000	2.1943	2.0181	1.3844	0.7616	0.3207	0.0543	0.0335	-0.0131	-0.0718
	93,000	2.2045	2.232	1.5155	1.1026	0.8281	0.3356	0.1622	0.0078	-0.0777
	5,000	1.9333	1.6676	1.2438	0.8238	0.3664	-0.0252	-0.0925	-0.0985	-0.1002
	9,000	1.7376	1.5476	1.2991	0.8612	0.3924	-0.0186	-0.0913	-0.0982	-0.1001
	21,000	1.8479	1.2586	0.6295	0.3466	0.0914	-0.0883	-0.0991	-0.1	-0.1004
32,000	39,000	1.8111	1.4779	0.9654	0.4603	0.0926	-0.0876	-0.099	-0.0999	-0.1004
	54,000	1.6903	1.5358	1.3301	1.1026	0.8388	0.3434	-0.0062	-0.0771	-0.0964
	68,000	1.6238	1.3773	1.1553	0.8537	0.3443	-0.0504	-0.0944	-0.0983	-0.1
	93,000	1.1052	0.9423	0.8638	0.6712	0.4958	0.2004	0.0802	-0.0246	-0.0843

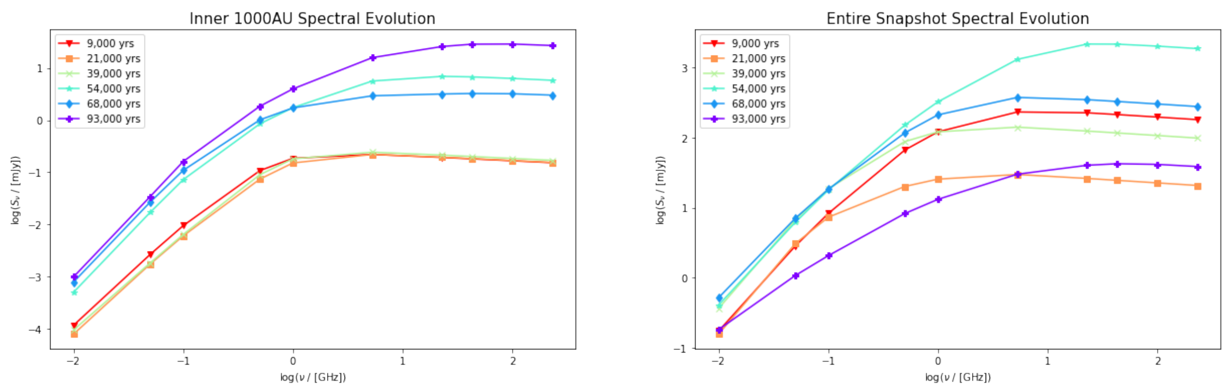

Figure 13. Time evolution of the spectral energy distribution in the 1000 au region (*left*) and the entire snapshot (*right*). The flux at each frequency from each snapshot (evolving in time from red to purple) is plotted vs. the frequency, both on a log scale. The spectral indices at each frequency, given as the slope between consecutive points in the plot, are given in 4 In the low frequency optically thick limit, the slope is expected to approach 2, while in the high frequency optically thin limit, the slope is expected to approach -.1.

then decrease, with the inner 1000 au region dropping to -.07 at 68,000 years, and the entire snapshot region dropping to -.08 at 93,000 years.

4. DISCUSSION

4.1. *Ionization Fraction*

Comparison of predicted observables to observations can shed light upon the validity of the simulated model for massive protostar formation, the Turbulent Core Model of formation by core accretion. The first comparison is between the average ionization fractions calculated by Fedriani et al. (2019) in the outflow of G35.2, shown in Figure 5. Since G35.2 consists of binary 11 and 6 $M_\odot$ stars, the comparison to the 8 and 12 $M_\odot$ snapshots in Fig. 5(c) and 5(d) are most relevant. In both, the emissivity weighted averages are above Fedriani et al.'s, which land among the volume and mass-weighted averages, depending on cutoff velocity. However, this is not a perfect comparison because the ionization fractions measured by Fedriani et al. were not characteristic values for the outflow, but rather from particularly bright knots. Thus, we expect them to be similar to the higher end of measured ionization fractions, and find our results to be consistent with this expectation. Further consideration as to what averaging method is most relevant to comparing

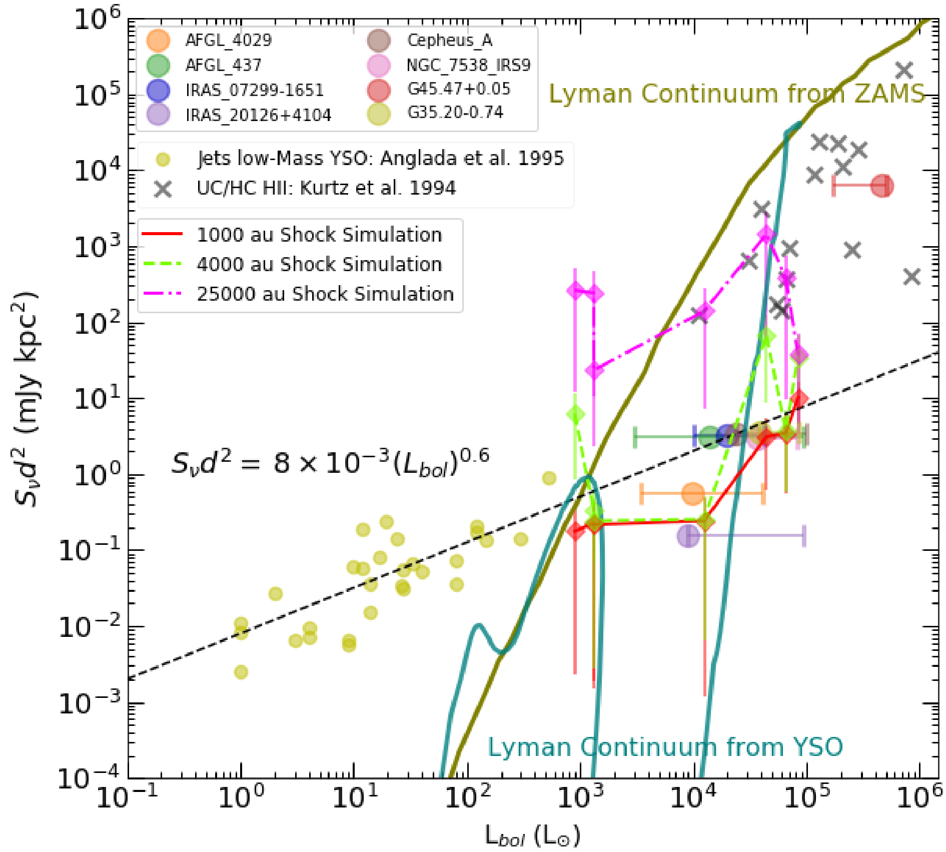

Figure 14. Radio luminosity vs. bolometric luminosity for the 5.3GHz shock emissions of our snapshots reaching 2, 4, 8, 12, 16, 24 $M_\odot$ at 9,000, 21,000, 39,000, 54,000, 68,000, and 94,000 years, respectively for the $-500\text{au} < x < 500\text{au}$, $0\text{au} < z < 1000au$ region in solid red, the $-2000\text{au} < x < 2000\text{au}$, $0\text{au} < z < 4000au$ region in dashed green and the entire snapshot in dash-dotted fuchsia. The radio luminosity $S_\nu d^2$ is calculated at a distance of $d = 1\text{kpc}$, for the fluxes given in 3 with error bars corresponding to their standard deviations. The large circles with horizontal error bars represent SOFIA Massive Star Formation Survey observations of massive protostars at 5 GHz (Rosero et al. 2019). The chartreuse smaller circles represent low-mass protostars observations ((Anglada 1995)) with their power law fit $8 \times 10^3 (L_{\text{bol}})^{.6}$ (Anglada et al. 2015). The $\times$'s portray observations of ultracompact HII regions from Kurtz et al. (1994). The solid dark green line portrays the Lyman continuum emission for a zero-age main sequence star predicted by Thompson (1984) and the solid teal line portrays the same for a massive protostar by Tanaka et al. (2016).

to ionization fraction is necessary for future comparisons to observations. This will depend on the methods by which observed ionization fractions are derived.

4.2. *Radio Emission*

The next result to be compared to observation is the predicted emissions, specifically radio luminosity vs. bolometric luminosity, as shown in Fig. 14. The inner 1000 au predictions from our simulation (in red) matched the SOMA observations of emissions from the inner 1000 au-radius region of eight massive protostars (Rosero et al. 2019), all of which landed near the low-mass protostar power-law fit by Anglada (1995). Thus, we can conclude that our simulation results are consistent with massive protostar observations, offering strong support for our model. Further, the correlation of both our shock simulation results and the SOMA massive star observations with the low-mass observations supports our proposition that massive stars form, like low-mass stars, through core accretion. Also, the shock-ionization simulation fills the gap in emissions predicted only by photo-ionization by Tanaka et al. (2016) in teal, in line with our assumption that shock-ionization from protostellar jets would be a predominant source of massive protostar emissions.

4.3. *Variability*

The average 10 year variability depicted in Fig. 10 can be compared to consecutive observations of massive star forming region W49A/G2 taken 20 years apart from De Pree et al. (2018). They found W49A/G2 to decrease in integrated flux by 40% between these two observations. This value was reached by the 230GHz percent variation calculated for the inner 1000, 2000, 4000, and 8000 au regions around 39,000 years, and exceeded the rest of the predicted variations. However, the time span was twice that of our variations, and W49A/G2's decrease was not necessarily characteristic of most massive protostars. Thus, it is reasonable that the 20 year W49A/G2 variation correspond to the peak values of 10 year variations predicted by our model. This does not provide convincing evidence for or against our model. Instead, we offer this variability data as a useful comparable for the near future, as new observations of massive protostars are made that we can compare with their counterparts from a decade ago.

4.4. *Caveats*

There are several caveats to our model to consider. For example, we used MHD snapshots to calculate an ionization fraction, but a time-dependent ionization fraction calculated continuously within the simulation would be more realistic. We also assumed adiabatic shocks, excluded self-absorption, and assumed that the shocked gas would flood the cell before cooling takes effect. It turns out that in some of the brightest regions, the cooling times are actually shorter than the shocked gas flow times, as shown in Fig. 1. To address this, the next step will be for us to account for cooling in our methods by scaling the depth over which we integrate for intensity by the ratio of $t_{\rm cool}/t_{\rm flow}$ within each cell. This would represent emissions only from the portion of gas flooded by the calculated shock temperature before cooling. Our data is also limited by resolution, and a comparison of our simulation to lower and higher resolution runs will be conducted in the future, to determine how resolution impacts our results.

5. SUMMARY & CONCLUSIONS

In summary, we present a model of shock-ionization for massive star formation. We modeled outputs relevant to observations including ionization fractions, radio fluxes and spectra, and variability properties. Initial comparison to observations of ionization fraction in the outflow of G35.2N (Fedriani et al. 2019); radio luminosity vs. bolometric luminosity of SOMA observations (Rosero et al. 2019), low-mass protostar observations (Anglada et al. 2015), and massive protostar photoionization models (Tanaka et al. 2016); and 20 year variation of W49A/G2 radio emissions (De Pree et al. 2018) offers support for the simulation, i.e., scaled up disk wind outflows in massive star formation. This research will be followed up by an investigation of how cooling effects and resolution impact our results.

I would like to thank Prof. Jonathan Tan, Prof. Jan Staff, and Dr. Jon Ramsey for their wise and supportive guidance as my research advisors throughout this project. I would also like to thank Dr. Rubén Fedriani for providing consult regarding his ionization fraction observations and Dr. Viviana Rosero for providing both her consult regarding the SOMA observations and code and data for the radio luminosity plot (Fig. 14). This research was initiated as an REU project with the Virginia Initiative on Cosmic Origins (VICO) summer research program, hosted by the Depts. of Astronomy, Chemistry, Computer Science, Environmental Sciences, and Materials Science & Engineering at the University of Virginia and the National Radio Astronomy Observatory, Charlottesville, VA, USA. This work was also supported by the National Science Foundation (NSF) project Protostellar Jets Across the Mass Spectrum (PJAMS). The authors acknowledge the use of the Rivanna computing cluster, under the management of Research Computing at the University of Virginia, to perform this research.

Software: Matplotlib (Hunter 2007), Jupyter (Kluyver et al. 2016)

REFERENCES

Anglada, G. 1995, in Revista Mexicana de Astronomia y Astrofisica Conference Series, Vol. 1, Revista Mexicana de Astronomia y Astrofisica Conference Series, ed. S. Lizano & J. M. Torrelles, 67

Anglada, G., Rodríguez, L. F., & Carrasco-Gonzalez, C. 2015, in Advancing Astrophysics with the Square Kilometre Array (AASKA14), 121. https://arxiv.org/abs/1412.6409

Arce, H. G., Shepherd, D., Gueth, F., et al. 2007, in Protostars and Planets V, ed. B. Reipurth, D. Jewitt, & K. Keil, 245. https://arxiv.org/abs/astro-ph/0603071

Bacciotti, F. 2004, Memorie della Societa Astronomica Italiana Supplementi, 5, 113

Blandford, R. D., & Payne, D. G. 1982, MNRAS, 199, 883, doi: 10.1093/mnras/199.4.883

Bonnell, I. A., Bate, M. R., Clarke, C. J., & Pringle, J. E. 1997, MNRAS, 285, 201, doi: 10.1093/mnras/285.1.201

De Pree, C. G., Galván-Madrid, R., Goss, W. M., et al. 2018, ApJL, 863, L9, doi: 10.3847/2041-8213/aad631

Fedriani, R., Caratti o Garatti, A., Purser, S. J. D., et al. 2019, Nature Communications, 10, 3630, doi: 10.1038/s41467-019-11595-x

Hunter, J. D. 2007, Computing in Science & Engineering, 9, 90, doi: 10.1109/MCSE.2007.55

Kluyver, T., Ragan-Kelley, B., Pérez, F., et al. 2016, in Positioning and Power in Academic Publishing: Players, Agents and Agendas, ed. F. Loizides & B. Schmidt, IOS Press, 87 – 90

Kurtz, S., Churchwell, E., & Wood, D. O. S. 1994, ApJS, 91, 659, doi: 10.1086/191952

McKee, C. F., & Tan, J. C. 2003, ApJ, 585, 850, doi: 10.1086/346149

Norman, M. L. 2000, in Revista Mexicana de Astronomia y Astrofisica Conference Series, Vol. 9, Revista Mexicana de Astronomia y Astrofisica Conference Series, ed. S. J. Arthur, N. S. Brickhouse, & J. Franco, 66–71. https://arxiv.org/abs/astro-ph/0005109

Rosero, V., Tanaka, K. E. I., Tan, J. C., et al. 2019, ApJL, 873, 21, doi: 10.3847/1538-4357/ab0209

Shu, F. H., Adams, F. C., & Lizano, S. 1987, ARA&A, 25, 23, doi: 10.1146/annurev.aa.25.090187.000323

Staff, J. E., Tanaka, K. E. I., & Tan, J. C. 2019, ApJ, 882, 123, doi: 10.3847/1538-4357/ab36b3

Tanaka, K. E. I., Tan, J. C., & Zhang, Y. 2016, ApJ, 818, 52, doi: 10.3847/0004-637X/818/1/52

Thompson, R. I. 1984, ApJ, 283, 165, doi: 10.1086/162287

Wang, P., Li, Z.-Y., Abel, T., & Nakamura, F. 2010, ApJ, 709, 27, doi: 10.1088/0004-637X/709/1/27

Zhang, Y., Tan, J. C., & Hosokawa, T. 2014, ApJ, 788, 166, doi: 10.1088/0004-637X/788/2/166